

# Six-fold crystalline anisotropic magnetoresistance in (111) $\text{LaAlO}_3/\text{SrTiO}_3$ oxide interface

P. K. Rout,<sup>†</sup> I. Agireen,<sup>†</sup> E. Maniv, M. Goldstein, and Y. Dagan<sup>1,\*</sup>

<sup>1</sup>Raymond and Beverly Sackler School of Physics and Astronomy, Tel-Aviv University, Tel Aviv, 69978, Israel  
(Dated: May 17, 2022)

We measured the magnetoresistance of the 2D electron liquid formed at the (111)  $\text{SrTiO}_3/\text{LaAlO}_3$  interface. The hexagonal symmetry of the interface is manifested in a six-fold crystalline component appearing in the anisotropic magnetoresistance (AMR) and planar Hall data, which agree well with symmetry analysis we performed. The six-fold component increases with carrier concentration, reaching 15% of the total AMR signal. Our results suggest that the coupling between higher itinerant electronic bands and the crystal as the origin of this effect, and demonstrate that (111) oxide interface is a unique hexagonal system with tunable magneto-crystalline effects.

*Introduction.*— The two dimensional electron liquid formed at the (100) interface between the two non-magnetic insulators  $\text{LaAlO}_3$  (LAO) and  $\text{SrTiO}_3$  (STO) [1] features numerous properties, such as superconductivity [2, 3] and spin-orbit coupling [4, 5], which are tunable by a gate voltage. Past studies have shown evidence for magnetic order (possibly co-existing with superconductivity) whose exact character is not yet clear [6–15], prompting much theoretical activity [16–18].

In-plane anisotropic magnetoresistance (AMR) can be employed as a probe for the magnetic properties of 2D structures, since it is sensitive to spin texture and spin-orbit interaction [19]. In the absence of crystalline anisotropy, rotating the magnetic field in the 2D plane results in a standard two-fold symmetric AMR term that depends on the angle between the magnetic field and the current. Such dependence has been observed in (100) LAO/STO [20–22]. It is absent in non-polar doped STO heterostructure [21] and can hence be related to the Rashba spin-orbit interaction which is expected to be less important in the latter. It has been suggested that an easy axis for magnetization can be observed in the AMR [18], however, the almost square symmetry of the interfacial crystal structure makes it difficult to distinguish between the two-fold term and the crystalline one. Here we explored a different interface, which has a hexagonal in-plane symmetry, namely the (111) LAO/STO heterostructure.

The stacking of (111) perovskite  $\text{ABO}_3$  layers is  $\text{AO}_3/\text{B}/\text{AO}_3/\text{B}$  [Fig. 1(a)], and therefore with alternating  $-3e$  and  $+3e$  charges in  $\text{LaAlO}_3$ , whereas  $-4e$  and  $+4e$  in  $\text{SrTiO}_3$  [23]. In addition to the different polar structure compared to (100) interface, its hexagonal symmetry has been predicted to be a key ingredient for the realization of various non-trivial states [24, 25]. Recently, six-fold Fermi-contour related to the symmetry of STO (111) surface has been observed by angle resolved photoemission [26, 27]. However, a distinct signature of six-fold symmetry of (111) LAO/STO interface is lacking. In this

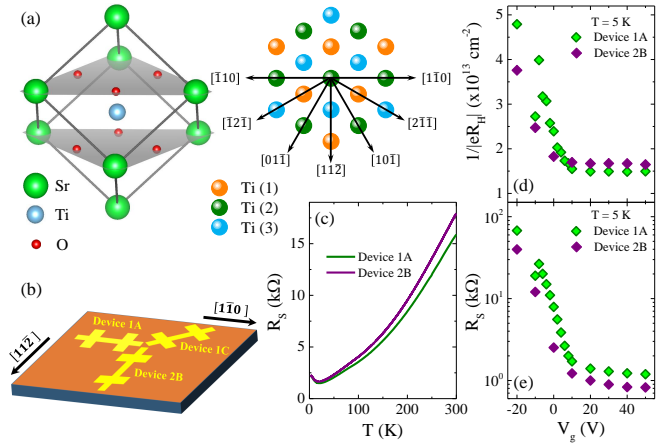


FIG. 1. (a) Left: Schematic depiction of  $\text{SrTiO}_3$  unit cell showing (111)  $(\text{SrO}_3)^{4-}$  planes. Right: Top view of three consecutive (111)  $\text{Ti}^{4+}$  planes showing various in-plane crystal directions. The Ti atoms in three different planes are marked as Ti(1) (orange), Ti(2) (green), and Ti(3) (blue). (b) Schematic of different  $100 \mu\text{m} \times 260 \mu\text{m}$  Hall bar devices oriented along  $[1\bar{1}0]$  (device 1A) and  $[1\bar{1}2]$  (device 2B). Device 1C lies at an angle of  $45^\circ$  to the other two. (c) Temperature dependent sheet resistance  $R_S(T)$  at  $V_g = 0$  V. (d,e) Gate dependence of the inverse Hall coefficient  $1/|eR_H|$  and sheet resistance  $R_S$  at  $T = 5$  K.

Letter we show theoretically and experimentally that a six-fold crystalline  $\cos(6\theta)$  term can be observed in the AMR of the (111) LAO/STO interface. This term depends on carrier concentration, suggesting that coupling between the lattice and higher energy itinerant electronic bands is an important ingredient for explaining magnetic effects in oxide interfaces.

*Methods.*— Epitaxial thin films of LAO were deposited on atomically flat Ti-terminated STO (111) substrate (substrate preparation is described in the Supplemental Material (SM) [28]) using pulsed laser deposition in oxygen partial pressure of  $1 \times 10^{-4}$  Torr at  $780^\circ\text{C}$ . After deposition the samples were annealed at  $400^\circ\text{C}$  in 0.2 Torr oxygen pressure for 1 hour. We followed a three step deposition process [S2] to fabricate Hall bars oriented along

\* yodagan@post.tau.ac.il; †P. K. R. and I. A. have contributed equally to this work

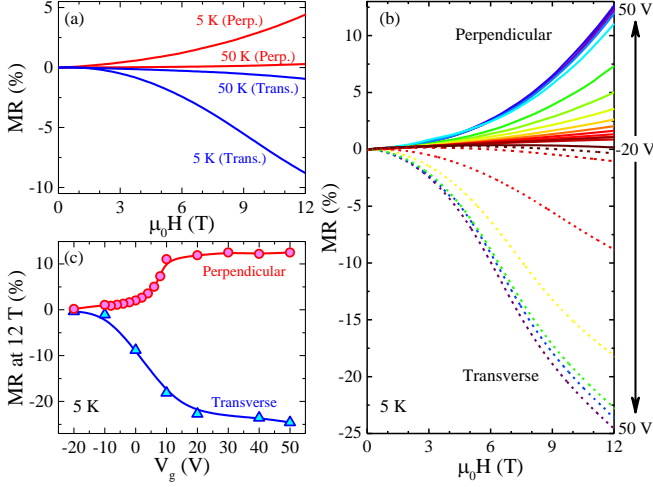


FIG. 2. Magnetoresistance for device 1A. (a) perpendicular ( $\vec{H}$  perpendicular to  $\vec{J}$  and interface) and transverse ( $\vec{H}$  perpendicular to  $\vec{J}$  and parallel to interface) magnetoresistance,  $MR = [R(H) - R(0)]/R(0)$ , at 5 K and 50 K ( $V_g = 0$  V). (b) MR as function of  $H$  at 5 K for different gate voltages. (c) MR at 12 T and 5 K as function of  $V_g$ .

different directions [Fig. 1(b)]. The thickness of LAO was 18  $\text{LaO}_3/\text{Al}$  layers (each layer is  $\approx 0.219$  nm thick). The typical sheet-resistance  $R_S(T)$  as a function of temperature for two different devices (1A and 2B) is shown in Fig. 1(c). Both devices exhibit similar metallic behavior with a residual resistance ratio  $R_S(300\text{ K})/R_S(10\text{ K})$  of 10 and resistance values of  $\sim 1.8$  k $\Omega$  at 10 K. Below 18 K both devices show a small upturn in  $R_S(T)$ , similar to Refs. [6, 30]. We have extracted the gate dependent Hall coefficients from low field Hall measurements [Fig. 1(d)]. The sign of the Hall voltage is consistent with electron-like carriers. Surprisingly,  $1/|eR_H|$  decreases when the gate voltage ( $V_g$ ) is raised from -20 V to 10 V. Upon increasing  $V_g$  further (up to 50 V) a saturation in  $1/|eR_H|$  is observed. The sheet resistance  $R_S(5\text{ K})$  also increases sharply when the  $V_g$  decreases below 10 V [Fig. 1(e)]. These observations are consistent with Ref. [31].

*Results.* — Fig. 2 shows the perpendicular ( $\vec{H}$  perpendicular to  $\vec{J}$  and interface) and transverse ( $\vec{H}$  perpendicular to  $\vec{J}$  and parallel to interface) magnetoresistance (MR) for device 1A. The data are symmetrized in the standard way. The orbital effect leads to positive perpendicular MR. By contrast, the transverse MR is negative, similar to Refs. [20, 32]. The MR values decrease monotonically with decreasing  $V_g$  as shown in Fig. 2(b). Both perpendicular and transverse MR values gradually rise with increasing gate till  $V_g = 10$  V and then saturate [Fig. 2(c)]. This saturation can be related to the saturation observed in  $R_S(V_g)$  and  $1/eR_H(V_g)$  [Fig. 1(d,e)].

We will now present the anisotropy in MR for two different angular rotations of the magnetic field. All these

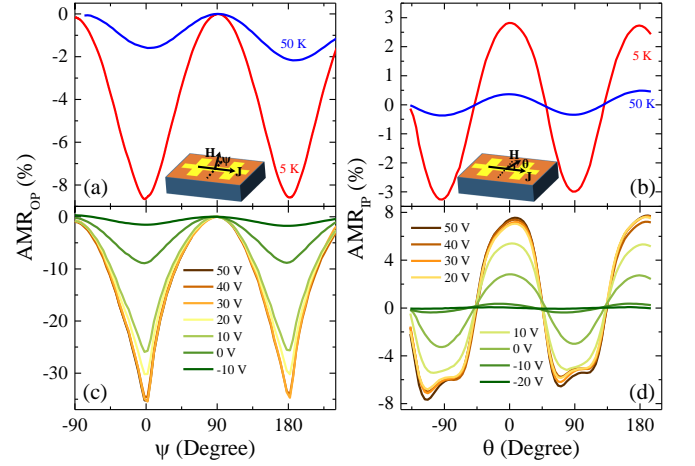


FIG. 3. AMR for device 1A. (a) Out-of-plane  $AMR_{OP}(\psi) = [R(\psi) - R(0)]/R(0)$ , at 5 K and 50 K for  $V_g = 0$  V.  $\psi$  is the angle between  $\vec{H}$  and the interface. (b) In-plane  $AMR_{IP}(\theta) = [R(\theta) - R_{mean}]/R_{mean}$  at 5 K and 50 K for  $V_g = 0$  V.  $R_{mean}$  is the angle-averaged resistance and  $\theta$  is the angle between  $\vec{H}$  and  $\vec{J}$ . (c,d) Gate dependence of  $AMR_{OP}(\psi)$  and  $AMR_{IP}(\theta)$  at 5 K. For high temperatures (e.g., 50 K) and low gates (e.g., -20 V),  $AMR_{IP}$  is maximal when  $\vec{H} \parallel \vec{J}$ . The corresponding angle is taken as  $\theta = 0^\circ$ .

measurements are performed at both positive and negative magnetic fields (i.e., +13.5 T and -13.5 T). Fig. 3(a,c) displays the out-of-plane  $AMR_{OP}$  for device 1A, which shows a maximum at  $\psi = 90^\circ$  and a sharper minimum at  $\psi = 0^\circ$ . We observe a maximum AMR amplitude of  $\approx 35\%$  for  $V_g = 50$  V, which starts decreasing with decreasing gate [Fig. 3(c)]. All these results are consistent with the MR data shown in Fig. 2. The in-plane  $AMR_{IP}$  for device 1A reveals a maximum at  $\theta = 0^\circ$  ( $\vec{H} \parallel \vec{J}$ ) and a minimum at  $\theta = 90^\circ$  ( $\vec{H} \perp \vec{J}$ ) [See Fig. 3(b)]. At negative gate voltage values the observed  $AMR_{IP}$  can be fitted with the standard twofold expression,  $C \cos(2\theta)$ . However, for positive gate voltages an increasing deviation from this two-fold behavior is observed [Fig. 3(d)]. To understand this unusual behavior, we employ symmetry considerations to calculate the form of the AMR for a 2D hexagonal lattice system up to order  $6\theta$  and find (see SM for details [28]):

$$AMR_{\text{hex}} = C_2 \cos(2\theta - 2\varphi) + C_4 \cos(4\theta + 2\varphi) + C_6 \cos(6\theta), \quad (1)$$

where  $C_2$ ,  $C_4$ , and  $C_6$  are two-, four-, and six-fold AMR coefficients, respectively.  $\theta$  ( $\varphi$ ) is the angle between  $\vec{H}$  ( $\vec{J}$ ) and the  $[1\bar{1}0]$  crystal axis. To verify the role of the six-fold symmetry, we have tried to fit the AMR data for device 1A ( $\varphi = 0^\circ$ ) with only two- and four-fold components [ $AMR_{Fit} = C_2 \cos(2\theta) + C_4 \cos(4\theta)$ ], and found clear deviations for positive gate voltages [the case  $V_g = 40$  V is shown in Fig. 4(a,c)]. The residual data ( $AMR_{IP} - AMR_{Fit}$ ) shows equally-spaced peaks separated by  $60^\circ$  [See Fig. 4(c)] — a clear six-fold structure,

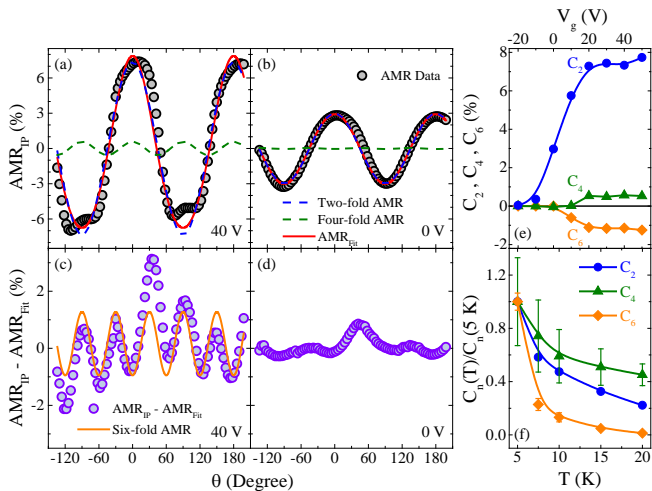


FIG. 4.  $AMR_{IP}$  at 5 K for  $V_g = 40$  V (a) and 0 V (b) measured on device 1A. The panels also include the two-fold and four-fold contributions, along with their sum,  $AMR_{Fit}$ . (c,d) The same data after subtracting  $AMR_{Fit}$  are shown along with six-fold fit. (e,f) Gate voltage (at 5 K) and temperature (at 0 V, sample I4 [28]) dependence of the AMR coefficients  $C_2$ ,  $C_4$ , and  $C_6$  [Eq. (1)].

which is well fitted by the last term of Eq. (1). Interestingly, we observe an additional contribution to AMR at  $30^\circ$  (and presumably at  $-150^\circ$ , which however is outside our rotator's range). This feature appears even  $V_g \leq 0$ , where the six-fold term is insignificant [Fig. 4(b,d)]; we discuss its origin below. Fig. 4(e,f) presents the AMR coefficients as function of gate voltage and temperature, respectively. It should be noted that  $|C_6| > |C_4|$ , as expected for a hexagonal crystal structure. Moreover,  $C_6$  appears at high gate voltages, and decays faster with temperature, as compared to  $C_2$ .

To further confirm that the AMR stems from the six-fold crystal structure, we measured it in two additional devices (1C and 1B), with different orientations with respect to the crystal axes ( $\varphi = 45^\circ$  and  $90^\circ$ , respectively), and performed a similar fit (Fig. 5). The residual data for all three devices show similar six-fold behavior [See Fig. 5(d-f)], which follows a  $C_6 \cos(6\theta)$  law, independent of  $\varphi$ , as expected for a 2D hexagonal system [Eq. (1)], indicating the crystalline nature of AMR. Our planar Hall data (Fig. S2 in [28]) also corroborates this picture. Let us note that such an angular dependence is inconsistent with square symmetry, as shown in the SM [28] (compare with [33]).

Fig. 5 also shows an additional uniaxial anisotropy lying along a crystal axis of the hexagonal system, similarly to Fig. 4(c,d). For devices 1A and 1C the anisotropy lies along the  $[2\bar{1}\bar{1}]$  direction, whereas it is along the  $[11\bar{2}]$  direction for device 2B, as shown in Fig. 5(g-i). The fact that these features can be seen at  $V_g \leq 0$  V, where the six-fold AMR is absent [Fig. 4(d)], implies that they have a different origin. One expects that the strong magnetic

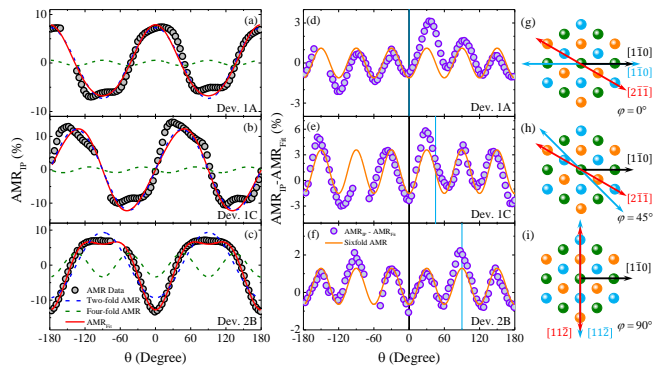


FIG. 5. (a-c)  $AMR_{IP}$  for device 1A (a) measured at 5 K while for devices 1C (b) and 2B (c) at 2 K. The applied gate voltage is  $V_g = 50$  V. The solid line shows the  $AMR_{Fit}$ , which is composed of two-fold and four-fold AMR contributions (dashed lines). The values of fitting parameter  $C_2$  are 7.7%, 12.2%, and 9.4% for devices 1A, 1C, and 2B, respectively, while the corresponding  $C_4$  values are 0.56%, 0.87%, and 3.45%. The data and fits are adjusted such that  $\theta = 0^\circ$  corresponds to the  $[1\bar{1}\bar{0}]$  direction. (d-f) The residual data ( $AMR_{IP} - AMR_{Fit}$ ) for devices 1A (d), 1C (e), and 2B (f) along with six-fold AMR fits (solid line). The vertical black line represents the  $[1\bar{1}\bar{0}]$  direction while the current direction is shown by vertical blue line. (g-i) Schematic of  $(111)$   $Ti^{4+}$  planes showing the  $[1\bar{1}\bar{0}]$  crystal axis (black arrow), current direction (blue arrow), and extra uniaxial anisotropy direction (red arrow) for the three devices.

field of 13.5 T, at which our AMR measurements were carried out, will be able to align all magnetic domains (if these exist) along the magnetic field direction, thus ruling out magnetic domain structure as an explanation. Another possibility is the presence of substrate terrace in Ti-terminated STO, which defines an anisotropy direction for conduction. However, the direction of the uniaxial component is not the same for our three devices, which were grown on the same substrate, thus eliminating this scenario as well. All this implies that the observed uniaxial AMR anisotropy should be related to structural domains in STO. Recently, anisotropic conductance has been observed in  $(001)$  LAO/STO [34, 35], which arises due to the formation of tetragonal domains in STO below 105 K. STO can have three different types of domains X, Y, and Z (distorted along the corresponding three principal directions of the original cubic lattice). These may form six boundary planes:  $(110)$  and  $(\bar{1}\bar{1}\bar{0})$  for X-Y,  $(011)$  and  $(0\bar{1}\bar{1})$  for Y-Z, and  $(101)$  and  $(10\bar{1})$  for Z-X [36]. These boundaries provide a low-resistance path, leading to anisotropy between the resistance in the parallel and perpendicular directions. In case of the  $(111)$  interface, these boundaries lie along  $[10\bar{1}]$  and  $[\bar{1}\bar{2}\bar{1}]$  for X-Y,  $[01\bar{1}]$  and  $[2\bar{1}\bar{1}]$  for Y-Z, and  $[1\bar{1}\bar{0}]$  and  $[11\bar{2}]$  for Z-X. Therefore, we can have six possible anisotropy directions depending upon the type of domain boundaries. It is plausible that our devices situated at different regions of STO will have different domain boundaries, and hence

different anisotropy directions. Interestingly, these structural domain boundaries manifest in the current response to a magnetic field.

Based on the above, one may then argue that by assuming that all six types of boundaries exist in equal proportions within the device, one could account for observed six-fold effect as well. However, as noted above, the six-fold effect and the uniaxial anisotropy appear in different gate voltage ranges. The sharp temperature dependence of the six-fold effect and its presence below 20 K [Fig. 4(f)] also disfavor structural domains as its origin. Finally, we have measured smaller ( $10\ \mu\text{m} \times 28\ \mu\text{m}$ ) Hall bar devices, and observed similar six-fold AMR (Fig. S4 in [28]). Since existence of an approximately “equal mixture” of the six boundaries between two voltage terminals in such a small device is highly unlikely, we conclude that the six-fold AMR is a manifestation of the six-fold anisotropy of the (111) plane of the undistorted cubic crystal.

*Discussion.*— What could then be the origin of the six-fold crystalline AMR? AMR necessitates spin-orbit interaction, and usually only appears in conjunction with magnetic order, typically ferromagnetic [37] (see however [38]). In (100) LAO/STO, strong and tunable spin-orbit interaction has been reported [4, 5] and related to AMR effects [21, 22]. However, the evidence for magnetic order at the temperature range of our experiment ( $T \geq 2\ \text{K}$ ) is elusive even for the better-studied (100) interface [6–15]: Magnetic hysteresis has been observed only below 1 K in a quasi-1D (100) system [15]. And our current measurements on (111) LAO/STO have shown no indication of magnetic order (e.g., no anomalous Hall effect or hysteresis) in the temperature range studied. Randomly-positioned magnetic dipoles have been observed in (100) LAO/STO [11, 12], which can account for the observations in the quasi-1D (100) case [15]. But it is unlikely that such scattered magnetic structure can account for the robust features we observe here with various device size and orientation.

The AMR coefficients  $C_2$  (standard AMR) and  $C_6$

(crystalline AMR) have strikingly different temperature and gate voltage dependences as well as opposite signs [Fig. 4(e,f)]. These findings suggest that they arise from different mechanisms. In a (111) heterostructure the titanium  $t_{2g}$  bands, which are believed to give rise to the 2D conduction, are split into two spin-3/2 bands and a spin-1/2 one [24, 25]. A natural possibility is therefore that  $C_6$  appears (as function of  $V_g$ ) upon the entrance of a higher band with stronger spin-orbit effects. One may speculate that such band is responsible for the change of slope in the gate dependence of the resistivity and Hall coefficient in the same  $V_g$  range [Fig. 1(d,e)].

It should be mentioned that Joshua *et al.* have reported that crystalline and non-crystalline AMR have different gate voltage dependence, and suggested that crystalline AMR is related to a Lifshitz transition in (100) LAO/STO [18] (see also [39]). On the other hand, by studying devices patterned along different crystal directions, Flekser *et al.* have found that all the AMR features depend only on  $\theta - \varphi$  (the angle between  $\vec{J}$  and  $\vec{H}$ ), indicating that AMR in the (100) system is non-crystalline [21]. This is very different from our current results for (111) LAO/STO, which have different dependence on  $\theta$  and  $\varphi$  [Fig. 5].

*Conclusion.*— To summarize, we utilize the unique hexagonal crystal symmetry of the (111) LAO/STO interface to provide a conclusive evidence for the crystalline nature of AMR in such oxide interfaces. We establish that the magnetic effects in this interface are firmly related to underlying crystal structure. The strong dependence of AMR on carrier concentration suggests that the itinerant electrons from higher energy bands couple strongly to the lattice and contribute to the magnetic effects.

*Acknowledgments.*— This work has been supported by the Israel Science Foundation (grants 569/13 and 227/15), the Israel Ministry of Science and Technology (contracts 3-11875 and 3-12419), and the Pazy Foundation (contract 268/17). P.K.R. acknowledges support from the Center for Nanosciences at Tel Aviv University.

- 
- [1] H. Y. Hwang, Y. Iwasa, M. Kawasaki, B. Keimer, N. Nagaosa, and Y. Tokura, *Nat. Mater.* **11**, 103 (2012).
  - [2] N. Reyren *et al.*, *Science* **317**, 1196 (2007).
  - [3] A. D. Caviglia *et al.*, *Nature* **456**, 624 (2008).
  - [4] M. Ben Shalom, M. Sachs, D. Rakhmievitch, A. Palevski, and Y. Dagan, *Phys. Rev. Lett.* **104**, 126802 (2010).
  - [5] A. D. Caviglia, M. Gabay, S. Gariglio, N. Reyren, C. Cancellieri, and J.-M. Triscone, *Phys. Rev. Lett.* **104**, 126803 (2010).
  - [6] A. Brinkman *et al.*, *Nature Mater.* **6**, 493 (2007).
  - [7] S. Seri and L. Klein, *Phys. Rev. B* **80**, 180410 (2009).
  - [8] M. Sachs, D. Rakhmievitch, M. B. Shalom, S. Shefler, A. Palevski, and Y. Dagan, *Physica C* **470**, S746 (2010).
  - [9] D. A. Dikin, M. Mehta, C. W. Bark, C. M. Folkman, C. B. Eom, and V. Chandrasekhar, *Phys. Rev. Lett.* **107**, 056802 (2011).
  - [10] L. Li, C. Richter, J. Mannhart, and R. C. Ashoori, *Nat. Phys.* **7**, 762 (2011).
  - [11] J. A. Bert, B. Kalisky, C. Bell, M. Kim, Y. Hikita, H. Y. Hwang, and K. A. Moler, *Nat. Phys.* **7**, 767 (2011).
  - [12] B. Kalisky, J. A. Bert, B. B. Klopfer, C. Bell, H. K. Sato, M. Hosoda, Y. Hikita, H. Y. Hwang, and K. A. Moler, *Nat. Commun.* **3**, 922 (2012).
  - [13] Z. Salman *et al.*, *Phys. Rev. Lett.* **109**, 257207 (2012).
  - [14] J. S. Lee, Y. W. Xie, H. K. Sato, C. Bell, Y. Hikita, H. Y. Hwang, and C. C. Kao, *Nat. Mater.* **12**, 703 (2013).
  - [15] A. Ron, E. Maniv, D. Graf, J.-H. Park, and Y. Dagan, *Phys. Rev. Lett.* **113**, 216801 (2014).
  - [16] K. Michaeli, A. C. Potter, and P. A. Lee, *Phys. Rev. Lett.* **108**, 117003 (2012).
  - [17] S. Banerjee, O. Erten, and M. Randeria, *Nat. Phys.* **9**, 626 (2013).

- [18] A. Joshua, J. Ruhman, S. Pecker, E. Altman, and S. Ilani, *Proc. Natl. Acad. Sci.* **110**, 9633 (2013).
- [19] M. Trushin, K. Výborný, P. Moraczewski, A. A. Kovalev, J. Schliemann, and T. Jungwirth, *Phys. Rev. B* **80**, 134405 (2009).
- [20] M. Ben Shalom, C. W. Tai, Y. Lereah, M. Sachs, E. Levy, D. Rakhmievitch, A. Palevski, and Y. Dagan, *Phys. Rev. B* **80**, 140403(R) (2009).
- [21] E. Flekser, M. Ben Shalom, M. Kim, C. Bell, Y. Hikita, H. Y. Hwang, and Y. Dagan, *Phys. Rev. B* **86**, 121104(R) (2012).
- [22] A. Fête, S. Gariglio, A. D. Caviglia, J.-M. Triscone, and M. Gabay, *Phys. Rev. B* **86**, 201105(R) (2012).
- [23] G. Herranz, F. Sanchez, N. Dix, M. Scigaj, and J. Fontcuberta, *Sci. Rep.* **2**, 758 (2012).
- [24] D. Xiao, W. Zhu, Y. Ran, N. Nagaosa, and S. Okamoto, *Nat. Commun.* **2**, 596 (2011).
- [25] D. Doennig, W. E. Pickett, and R. Pentcheva, *Phys. Rev. Lett.* **111**, 126804 (2013).
- [26] T. C. Rödel, C. Bareille, F. Fortuna, C. Baumier, F. Bertran, P. Le Fèvre, M. Gabay, O. H. Cubelos, M. J. Rozenberg, T. Maroutian, P. Lecoeur, and A. F. Santander-Syro, *Phys. Rev. Applied* **1**, 051002 (2014).
- [27] S. McKeown Walker, A. de la Torre, F. Y. Bruno, A. Tamai, T. K. Kim, M. Hoesch, M. Shi, M. S. Bahramy, P. D. C. King, and F. Baumberger, *Phys. Rev. Lett.* **113**, 177601 (2014).
- [28] See Supplemental Material
- [29] E. Maniv, M. B. Shalom, A. Ron, M. Mograbi, A. Palevski, M. Goldstein, and Y. Dagan, *Nat. Commun.* **6**, 8239 (2015).
- [30] J. Biscaras, N. Bergeal, A. Kushwaha, T. Wolf, A. Rastogi, R. C. Budhani, and J. Lesueur, *Nature Commun.* **1**, 89 (2010).
- [31] Samuel Davis, V. Chandrasekhar, Z. Huang, K. Han, Ariando, and T. Venkatesan, arXiv:1603.04538v2.
- [32] M. Diez, A. M. R. V. L. Monteiro, G. Mattoni, E. Cobanera, T. Hyart, E. Mulazimoglu, N. Bovenzi, C. W. J. Beenakker, and A. D. Caviglia, *Phys. Rev. Lett.* **115**, 016803 (2015).
- [33] J. H. Ngai, Y. Segal, F. J. Walker, and C. H. Ahn, *Phys. Rev. B* **83**, 045304 (2011).
- [34] B. Kalisky *et al.*, *Nat. Mater.* **12**, 1091 (2013).
- [35] Y. Frenkel, N. Haham, Y. Shperber, C. Bell, Y. Xie, Z. Chen, Y. Hikita, H. Y. Hwang, and B. Kalisky, *ACS Appl. Mater. Interfaces* **8**, 12514 (2016).
- [36] M. Honig, J. A. Sulpizio, J. Drori, A. Joshua, E. Zeldov, and S. Ilani, *Nat. Mater.* **12**, 1112 (2013).
- [37] T. R. McGuire and R. I. Potter, *IEEE Trans. Magn.* **11**, 1018 (1975).
- [38] I. Genish, Y. Kats, L. Klein, J. W. Reiner, and M. R. Beasley, *J. Appl. Phys.* **95**, 6681 (2004).
- [39] A. Annadi, Z. Huang, K. Gopinadhan, X. R. Wang, A. Srivastava, Z. Q. Liu, H. H. Ma, T. P. Sarkar, T. Venkatesan, and Ariando, *Phys. Rev. B* **87**, 201102 (2013).

## SUPPLEMENTAL MATERIAL

In the Supplementary Material we provide details on our substrate preparation procedure (Sec. S1), derive expressions for the anisotropic magnetoresistance (AMR) and planar Hall effect (PHE) up to order  $6\theta$  for 2D systems with either hexagonal or square symmetry (Sec. S2), and present PHE data (Sec. S3) as well as results on an additional large device in comparison with a small one (Sec. S4).

### S1. SUBSTRATE PREPARATION

The surface treatment to obtain atomically flat Ti-terminated STO (111) consisted of combined chemical etching and annealing process. In the first step, unterminated  $5 \times 5 \text{ mm}^2$  STO (111) substrates were soaked in DI water for 30 minutes and subsequently annealed at  $950^\circ\text{C}$  in oxygen for 3 hours. After soaking another 30 minutes in DI water with 10 min ultrasonic agitation, the substrates were dipped in buffered HF solution for 10 sec. Finally, the substrates were annealed at  $950^\circ\text{C}$  in oxygen for 2 hours. Out of many trials, we were able to obtain few atomically smooth Ti-terminated substrates. Fig. S1 displays typical AFM image of a smooth substrate, which clearly shows the step and terrace structure with step heights of  $2.2 \text{ \AA}$ , matching the inter-planar distance of two consecutive Ti-layers in the [111]-direction.

### S2. ANISOTROPIC MAGNETORESISTANCE AND PLANAR HALL EFFECT IN SQUARE AND HEXAGONAL 2D CRYSTALS

The symmetric part of the 2D resistivity tensor in the presence of an in-plane magnetic field directed along a unit vector  $\vec{\alpha} = (\alpha_1, \alpha_2) \equiv (\cos \theta, \sin \theta)$  at an angle  $\theta$  relative to some reference crystal axis, can be expressed as a series expansion in  $\alpha_i$  [S1]:

$$\rho_{ij}(\vec{\alpha}) = a_{ij} + a_{klij}\alpha_k\alpha_l + a_{klmni j}\alpha_k\alpha_l\alpha_m\alpha_n + a_{klmnpqij}\alpha_k\alpha_l\alpha_m\alpha_n\alpha_p\alpha_q + \dots \quad (\text{S1})$$

This tensor is even in the magnetic field, and hence, due to Onsager's relations, is symmetric in the indices  $i, j$ . By definition, each term in the expansion is symmetric under any interchange of the indices  $k, l, \dots$ . Therefore, the value of each coefficient  $a_{kl\dots ij}$  only depends on how many of the indices  $i, j$  and how many of the indices  $k, l, \dots$  equal 1 or 2 ( $x$  or  $y$ , respectively).

For current  $\vec{J}$  directed along the unit vector  $\vec{\beta} = (\beta_1, \beta_2) \equiv (\cos \varphi, \sin \varphi)$  at an angle  $\varphi$  relative to the reference crystal axis, the longitudinal resistance is given by

$$\rho_L(\vec{\alpha}, \vec{\beta}) = \rho_{ij}(\vec{\alpha})\beta_i\beta_j, \quad (\text{S2})$$

whereas the planar hall effect can be expressed as:

$$\rho_{PH}(\vec{\alpha}, \vec{\beta}) = \rho_{ij}(\vec{\alpha})\beta'_i\beta_j, \quad (\text{S3})$$

where  $\vec{\beta}' = (-\beta_2, \beta_1)$  is a unit vector perpendicular to  $\vec{J}$ . We now present our results for these quantities in 2D square and hexagonal crystals up to order  $6\theta$  (previous calculations only went up to  $4\theta$  [S1]).

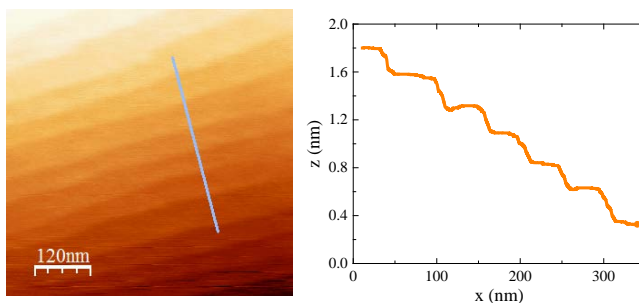


FIG. S1. Left panel: AFM image of an atomically smooth STO (111) surface displaying step and terrace structure. Right panel: A cut across the steps marked by the line in the AFM image.

### A. 2D square crystal

For a 2D square crystal (space group **p4m** / point group  $D_4$ ), the non-vanishing coefficients in Eq. (S1) and the relation between them are determined from symmetry analysis of  $\rho_{ij}$  and are given in Tables S1-S4. Reflection about the  $x$  ( $y$ ) axis flips the 1 (2) component of electric field (polar vector; indices  $i, j$ ), and the 2 (1) component of the magnetic field (axial vector; indices  $k, l, \dots$ ). Thus, by the *mirror* symmetries, only coefficients with an even number of the indices  $i, j, k, l, \dots$  equal to 1 and even number equal to 2 do not vanish. In addition, the  $90^\circ$  *rotation* symmetry implies that interchanging the values of all the indices between 1 and 2 do not change the value of the coefficient; for example,  $a_{11111212} = a_{12222212}$ . Combining these findings with the fact that the order of the indices  $i, j$  or  $k, l, \dots$  in Eq. (S1) is irrelevant, as discussed above, we find the results summarized in the Tables below.

TABLE S1.  $a_{ij}$  from Eq. (S1) for 2D square and hexagonal crystals.

$\beta_i\beta_j$	$\beta_1^2$	$\beta_2^2$	$\beta_1\beta_2$	$\beta_2\beta_1$
$\bar{i}\bar{j}$	11	11		

TABLE S2.  $a_{ijkl}$  from Eq. (S1) for 2D square and hexagonal crystals.

$\alpha_k\alpha_l$ \ $\beta_i\beta_j$	$\beta_1^2$	$\beta_2^2$	$\beta_1\beta_2$	$\beta_2\beta_1$
$\alpha_1^2$	1111	1122		
$\alpha_2^2$	1122	1111		
$\alpha_1\alpha_2$			1212	1212

TABLE S3.  $a_{ijklmn}$  from Eq. (S1) for a 2D square crystal.

$\alpha_k\alpha_l\alpha_m\alpha_n$ \ $\beta_i\beta_j$	$\beta_1^2$	$\beta_2^2$	$\beta_1\beta_2$	$\beta_2\beta_1$
$\alpha_1^4$	111111	111122		
$\alpha_2^4$	111122	111111		
$\alpha_1^3\alpha_2$			111212	111212
$\alpha_1^2\alpha_2^2$	112211	112211		
$\alpha_1\alpha_2^3$			111212	111212

TABLE S4.  $a_{ijklmnpq}$  from Eq. (S1) for a 2D square crystal.

$\alpha_k\alpha_l\alpha_m\alpha_n\alpha_p\alpha_q$ \ $\beta_i\beta_j$	$\beta_1^2$	$\beta_2^2$	$\beta_1\beta_2$	$\beta_2\beta_1$
$\alpha_1^6$	11111111	11111122		
$\alpha_2^6$	11111122	11111111		
$\alpha_1^4\alpha_2^2$	11112211	11222211		
$\alpha_1^2\alpha_2^4$	11222211	11112211		
$\alpha_1^5\alpha_2$			11111212	11111212
$\alpha_1^3\alpha_2^3$			11122212	11122212
$\alpha_1\alpha_2^5$			11111212	11111212

The longitudinal resistivity can thus be written as

$$\begin{aligned}
\rho_L(\vec{\alpha}, \vec{\beta}) = & a_{11} + a_{1111}(\alpha_1^2\beta_1^2 + \alpha_2^2\beta_2^2) + a_{1122}(\alpha_1^2\beta_2^2 + \alpha_2^2\beta_1^2) + 4a_{1212}\alpha_1\alpha_2\beta_1\beta_2 \\
& + a_{111111}(\alpha_1^4\beta_1^2 + \alpha_2^4\beta_2^2) + a_{111122}(\alpha_1^4\beta_2^2 + \alpha_2^4\beta_1^2) + 6a_{112211}\alpha_1^2\alpha_2^2 + 8a_{111212}\alpha_1\alpha_2\beta_1\beta_2 \\
& + a_{11111111}(\alpha_1^6\beta_1^2 + \alpha_2^6\beta_2^2) + a_{11111122}(\alpha_1^6\beta_2^2 + \alpha_2^6\beta_1^2) + 15a_{11112211}(\alpha_1^4\alpha_2^2\beta_1^2 + \alpha_1^2\alpha_2^4\beta_2^2) \\
& + 15a_{11222211}(\alpha_1^4\alpha_2^2\beta_2^2 + \alpha_1^2\alpha_2^4\beta_1^2) + 12a_{11111212}(\alpha_1^5\alpha_2 + \alpha_1\alpha_2^5)\beta_1\beta_2 + 40a_{11122212}\alpha_1^3\alpha_2^3\beta_1\beta_2, \quad (S4)
\end{aligned}$$

or, in terms of  $\theta$  and  $\varphi$ ,

$$\rho_L(\theta, \varphi) = C'_0 + C'_2 \cos(2\theta) \cos(2\varphi) + S'_2 \sin(2\theta) \sin(2\varphi) + C'_4 \cos(4\theta) + C'_6 \cos(6\theta) \cos(2\varphi) + S'_6 \sin(6\theta) \sin(2\varphi), \quad (S5)$$

where

$$\begin{aligned}
C'_0 &= a_{11} + \frac{1}{2}(a_{1111} + a_{1122}) + \frac{3}{8}(a_{111111} + a_{111122} + 2a_{112211}) + \frac{5}{16}(a_{11111111} + a_{11111122} + 3a_{11112211} + 3a_{11222211}), \\
C'_2 &= \frac{1}{2}(a_{1111} - a_{1122}) + \frac{1}{2}(a_{111111} - a_{111122}) + \frac{15}{32}(a_{11111111} - a_{11111122} + a_{11112211} - a_{11222211}), \\
S'_2 &= a_{1212} + 2a_{111212} + \frac{15}{8}(a_{11111212} + a_{11122212}), \\
C'_4 &= \frac{1}{8}(a_{11111111} + a_{11111122} - 6a_{112211}) + \frac{3}{16}(a_{1111111111} + a_{1111111122} - 5a_{1111112211} - 5a_{11222211}), \\
C'_6 &= \frac{1}{32}(a_{1111111111} - a_{1111111122} - 15a_{1111112211} + 15a_{11222211}), \\
S'_6 &= \frac{1}{8}(3a_{11111212} - 5a_{11122212}).
\end{aligned}$$

Thus, the AMR can be expressed as

$$\text{AMR}_{\text{sq}} = C_2 \cos(2\theta) \cos(2\varphi) + S_2 \sin(2\theta) \sin(2\varphi) + C_4 \cos(4\theta) + C_6 \cos(6\theta) \cos(2\varphi) + S_6 \sin(6\theta) \sin(2\varphi), \quad (\text{S6})$$

where  $C_2$ ,  $S_2$ ,  $C_4$ ,  $C_6$ , and  $S_6$  are, respectively,  $C'_2$ ,  $S'_2$ ,  $C'_4$ ,  $C'_6$ , and  $S'_6$  divided by mean resistivity  $C'_0$ . The corresponding expression for the PHE is

$$\text{PHE}_{\text{sq}} = -C_2 \cos(2\theta) \sin(2\varphi) + S_2 \sin(2\theta) \cos(2\varphi) - C_6 \cos(6\theta) \sin(2\varphi) + S_6 \sin(6\theta) \cos(2\varphi). \quad (\text{S7})$$

## B. 2D hexagonal crystal

For a 2D hexagonal crystal (space group **p6m** / point group  $D_6$ ), the non-vanishing coefficients in Eq. (S1) and the relations between them are given in Tables S1, S2, S5, and S6. As in the square case, only coefficients with an even number of indices equal to 1 and even number equal to 2 do not vanish due to *mirror* symmetry. In addition,  $60^\circ$  *rotation* symmetry implies that [S1]:

$$a_{ijkl\dots} = \sigma_{ip}\sigma_{jq}\sigma_{kr}\sigma_{ls\dots}a_{pqrs\dots}, \quad (\text{S8})$$

where

$$\sigma = \begin{pmatrix} \frac{1}{2} & -\frac{\sqrt{3}}{2} \\ \frac{\sqrt{3}}{2} & \frac{1}{2} \end{pmatrix}. \quad (\text{S9})$$

which leads to the following relations:

$$a_{1111} = a_{1122} + 2a_{1212}, \quad (\text{S10})$$

as well as

$$\begin{aligned}
a_{111122} &= 2a_{111111} + 6a_{112211} - 3a_{222222}, \\
a_{112222} &= a_{111111} + a_{112211} - a_{222222}, \\
a_{222211} &= 3a_{111111} + 6a_{112211} - 4a_{222222}, \\
a_{111212} &= -a_{111111} - \frac{3}{2}a_{112211} + \frac{3}{2}a_{222222}, \\
a_{122212} &= -\frac{3}{2}a_{112211} + \frac{1}{2}a_{222222},
\end{aligned} \quad (\text{S11})$$

TABLE S5.  $a_{ijklmn}$  from Eq. (S1) for a 2D hexagonal crystal.

$\alpha_k \alpha_l \alpha_m \alpha_n$ \diagdown $\beta_i \beta_j$	$\beta_1^2$	$\beta_2^2$	$\beta_1 \beta_2$	$\beta_2 \beta_1$
$\alpha_1^4$	111111	111122		
$\alpha_2^4$	222211	222222		
$\alpha_1^3 \alpha_2$			111212	111212
$\alpha_1^2 \alpha_2^2$	112211	112222		
$\alpha_1 \alpha_2^3$			122212	122212

TABLE S6.  $a_{ijklmnpq}$  from Eq. (S1) for a 2D hexagonal crystal.

$\alpha_k \alpha_l \alpha_m \alpha_n \alpha_p \alpha_q$ \diagdown $\beta_i \beta_j$	$\beta_1^2$	$\beta_2^2$	$\beta_1 \beta_2$	$\beta_2 \beta_1$
$\alpha_1^6$	11111111	11111122		
$\alpha_2^6$	22222211	22222222		
$\alpha_1^4 \alpha_2^2$	11112211	11112222		
$\alpha_1^2 \alpha_2^4$	11222211	11222222		
$\alpha_1^5 \alpha_2$			11111212	11111212
$\alpha_1^3 \alpha_2^3$			11122212	11122212
$\alpha_1 \alpha_2^5$			12222212	12222212

and

$$\begin{aligned}
15a_{11222211} &= 3a_{11111111} + 6a_{11111122} - 4a_{22222211} - 2a_{22222222}, \\
15a_{11222222} &= 6a_{11111111} + 3a_{11111122} - 2a_{22222211} - 4a_{22222222}, \\
15a_{11112211} &= -4a_{11111111} - 2a_{11111122} + 3a_{22222211} + 6a_{22222222}, \\
15a_{11112222} &= -2a_{11111111} - 4a_{11111122} + 6a_{22222211} + 3a_{22222222}, \\
12a_{11111212} &= -a_{11111111} + a_{11111122} - 3a_{22222211} + 3a_{22222222}, \\
20a_{11122212} &= a_{11111111} - a_{11111122} - a_{22222211} + a_{22222222}, \\
12a_{12222212} &= 3a_{11111111} - 3a_{11111122} + a_{22222211} - a_{22222222}.
\end{aligned} \tag{S12}$$

As a result of all this, the longitudinal resistivity can be written as

$$\begin{aligned}
\rho_L(\vec{\alpha}, \vec{\beta}) &= a_{11} + a_{1111}(\alpha_1^2 \beta_1^2 + \alpha_2^2 \beta_2^2) + a_{1122}(\alpha_1^2 \beta_2^2 + \alpha_2^2 \beta_1^2) + 4a_{1212} \alpha_1 \alpha_2 \beta_1 \beta_2 + a_{111111} \alpha_1^4 \beta_1^2 + a_{111122} \alpha_1^4 \beta_2^2 \\
&+ a_{222211} \alpha_2^4 \beta_1^2 + a_{222222} \alpha_2^4 \beta_2^2 + 6a_{112211} \alpha_1^2 \alpha_2^2 \beta_1^2 + 6a_{112222} \alpha_1^2 \alpha_2^2 \beta_2^2 + 8a_{111212} \alpha_1^3 \alpha_2 \beta_1 \beta_2 + 8a_{122212} \alpha_1 \alpha_2^3 \beta_1 \beta_2 \\
&+ a_{11111111} \alpha_1^6 \beta_1^2 + a_{11111122} \alpha_1^6 \beta_2^2 + a_{22222211} \alpha_2^6 \beta_1^2 + a_{22222222} \alpha_2^6 \beta_2^2 + 15a_{11112211} \alpha_1^4 \alpha_2^2 \beta_1^2 + 15a_{11112222} \alpha_1^4 \alpha_2^2 \beta_2^2 \\
&+ 15a_{11222211} \alpha_1^2 \alpha_2^4 \beta_1^2 + 15a_{11222222} \alpha_1^2 \alpha_2^4 \beta_2^2 + 12a_{11111212} \alpha_1^5 \alpha_2 \beta_1 \beta_2 + 40a_{11122212} \alpha_1^3 \alpha_2^3 \beta_1 \beta_2 + 12a_{12222212} \alpha_1 \alpha_2^5 \beta_1 \beta_2,
\end{aligned} \tag{S13}$$

or in terms of  $\theta$  and  $\varphi$ ,

$$\rho_L(\theta, \varphi) = C'_0 + C'_2 [\cos(2\theta) \cos(2\varphi) + \sin(2\theta) \sin(2\varphi)] + C'_4 [\cos(4\theta) \cos(2\varphi) - \sin(4\theta) \sin(2\varphi)] + C'_6 \cos(6\theta), \tag{S14}$$

where

$$\begin{aligned}
C'_0 &= a_{11} + \frac{1}{2}(a_{1111} + a_{1122}) + \frac{1}{2}(3a_{111111} + 6a_{112211} - 3a_{222222}) + \frac{1}{4}(a_{11111111} + a_{11111122} + a_{22222211} + a_{22222222}), \\
C'_2 &= \frac{1}{4}(a_{1111} - a_{1122} + 2a_{1212}) + \frac{1}{2}(-2a_{111111} - 6a_{112211} + 4a_{222222}) + \frac{1}{4}(a_{11111111} - a_{11111122} - a_{22222211} + a_{22222222}), \\
C'_4 &= \frac{1}{2}(a_{111111} - a_{222222}) + \frac{1}{4}(a_{11111111} - a_{11111122} + a_{22222211} - a_{22222222}), \\
C'_6 &= \frac{1}{4}(a_{11111111} + a_{11111122} - a_{22222211} - a_{22222222}).
\end{aligned}$$

Thus, the AMR can be expressed as

$$\text{AMR}_{\text{hex}} = C_2 [\cos(2\theta) \cos(2\varphi) + \sin(2\theta) \sin(2\varphi)] + C_4 [\cos(4\theta) \cos(2\varphi) - \sin(4\theta) \sin(2\varphi)] + C_6 \cos(6\theta) \tag{S15}$$

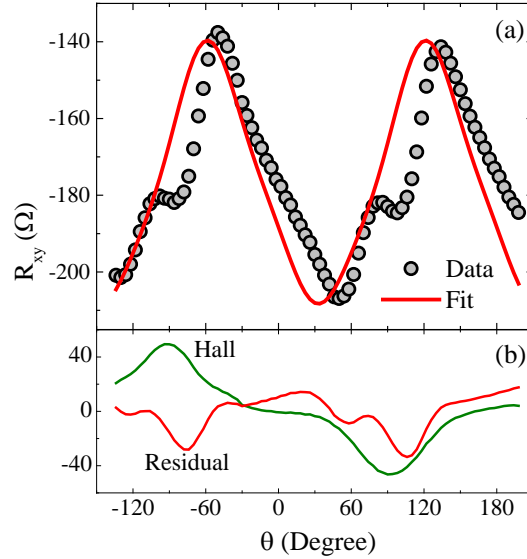


FIG. S2. (a) The transverse resistance  $R_{xy}$  of device 1A measured at  $H = 13.5$  T,  $V_g = 40$  V and  $T = 5$  K. The solid line is a best fit to  $[\text{PHE}_{\text{hex}} \cos \epsilon + (1 + \text{AMR}_{\text{hex}}) \sin \epsilon] R_{L,\text{mean}}$  with  $\epsilon = -9.1^\circ$  (see the text for more details). (b) The residual of the fit to the PHE data and the field-antisymmetric part of  $R_{xy}$  (normal Hall contribution).

where  $C_2$ ,  $C_4$ , and  $C_6$  are, respectively,  $C'_2$ ,  $C'_4$ , and  $C'_6$  divided by the mean resistivity  $C'_0$ . The corresponding expression for the PHE is

$$\text{PHE}_{\text{hex}} = -C_2 [\cos(2\theta) \sin(2\varphi) - \sin(2\theta) \cos(2\varphi)] - C_4 [\cos(4\theta) \sin(2\varphi) + \sin(4\theta) \cos(2\varphi)]. \quad (\text{S16})$$

Interestingly, the six-fold term drops out of the PHE in a hexagonal crystal.

### S3. PHE MEASUREMENT

Fig. S2(a) presents a typical PHE curve at  $V_g = 40$  V for device 1A after symmetrization of the data measured at  $+13.5$  T and  $-13.5$  T. The nonzero average value of the PHE indicates the presence of some longitudinal resistance due to contact misalignment. Therefore, the data can be assumed to be a linear combination of the PHE and AMR,  $[\text{PHE}_{\text{hex}} \cos \epsilon + (1 + \text{AMR}_{\text{hex}}) \sin \epsilon] R_{L,\text{mean}}$ , where  $\text{AMR}_{\text{hex}}$  and  $\text{PHE}_{\text{hex}}$  are given by Eqs. (S15) and (S16), respectively.  $\epsilon$  represents the misalignment angle, whereas  $R_{L,\text{mean}}$  is the angle-averaged longitudinal resistance. Using the  $R_{L,\text{mean}}$  and  $C_n$  obtained from the fit of the AMR data (cf. Fig. 4 of main text), we can get a reasonably good fit to the PHE data with a single fitting parameter  $\epsilon$ . We do see relatively large deviations near  $-80^\circ$  and  $100^\circ$ . However, these positions coincide with the region where the antisymmetric part with respect to the magnetic field (normal Hall contribution) of  $R_{xy}$  is large [see Fig. S2(b)]. This Hall signal can arise from small perpendicular field due to a wobble of the probe. Hence, we believe that the observed deviation of the PHE is related to instrumental artifacts. In principle, the perpendicular field could have also modified the AMR data. However, extracting the perpendicular magnetic field from the Hall data in Fig. S2(b), we find the corresponding perpendicular MR values to be less than 0.2%. Therefore, the AMR data is practically insensitive to the wobble, and for this reason we concentrated on it for the analysis presented in the main text.

### S4. ADDITIONAL IN-PLANE AMR MEASUREMENTS

We present the in-plane AMR data of two more LAO/STO (111) devices. Sample I3 is similar to the sample mentioned in the main text, and was accordingly prepared using a three step deposition process (as described in Ref. [S2]), while a single step deposition process was employed to fabricate a smaller ( $10 \mu\text{m} \times 28 \mu\text{m}$ ) Hall bar devices on sample I4 [S3].

Fig. S3 displays the  $\text{AMR}_{IP}$  for a device on sample I3 which is oriented along  $[1\bar{1}0]$  for positive gate voltages. We can see equispaced peaks separated by  $60^\circ$  in the residual  $\text{AMR}_{IP} - \text{AMR}_{Fit}$  due to hexagonal symmetry, which is

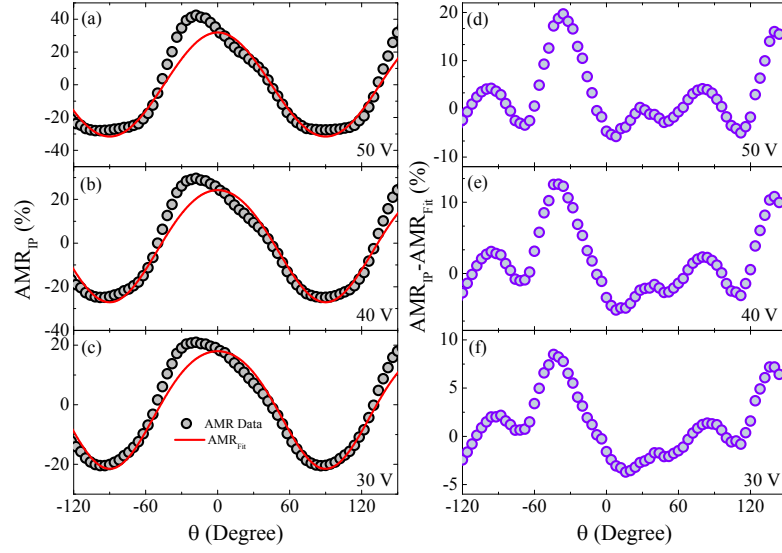


FIG. S3.  $AMR_{IP}$  measured on  $100 \mu\text{m} \times 260 \mu\text{m}$  Hall bar device (sample I3) oriented along  $[1\bar{1}0]$  at 5 K for  $V_g = 50 \text{ V}$  (a), 40 V (b), and 30 V (c). The corresponding residuals are shown in (d-f).

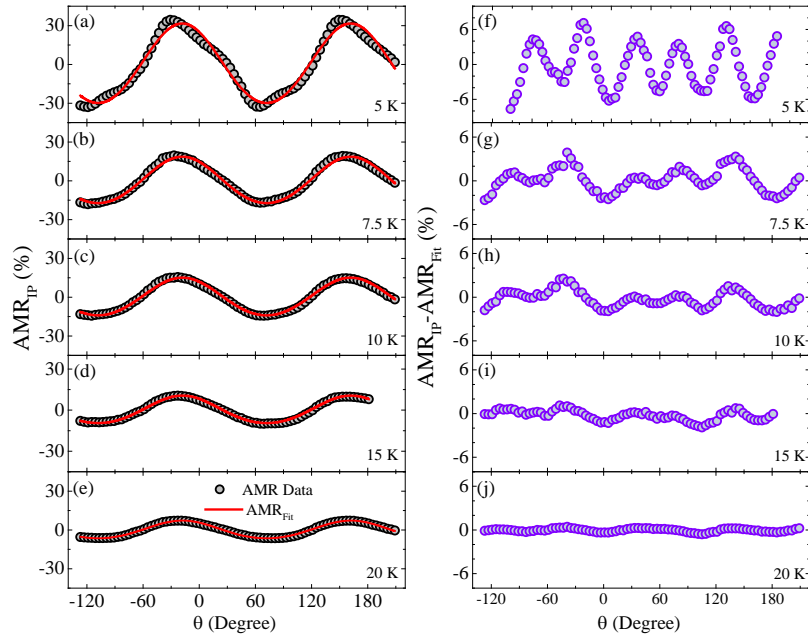


FIG. S4. The  $AMR_{IP}$  measured on a smaller  $10 \mu\text{m} \times 28 \mu\text{m}$  Hall bar (sample I4) oriented along  $[1\bar{1}0]$  at  $V_g = 0 \text{ V}$  for  $T = 5 \text{ K}$  (a), 7.5 K (b), 10 K (c), 15 K (d), and 20 K (e). The corresponding residuals are presented in (f-j).

quite similar to the results shown in the main text. The  $AMR_{IP}$  data of the smaller device on sample I4 oriented along  $[1\bar{1}0]$  for various temperatures are presented in Fig. S4. It displays a similar behavior to the larger device, thus ruling out structural domains as the origin of the six-fold effect, as explained in the main text. The temperature dependence of the AMR coefficients for the last device is displayed in Fig. 4(f) of the main text.

[S1] R. R. Birss, *Symmetry and Magnetism*, (North-Holland, Amsterdam, 1964).

[S2] E. Maniv, M. B. Shalom, A. Ron, M. Mograbi, A. Palevski, M. Goldstein, and Y. Dagan, Nat. Commun. **6**, 8239 (2015).

[S3] E. Maniv, A. Ron, M. Goldstein, A. Palevski, and Y. Dagan, Phys. Rev. B **94**, 045120 (2016).